Astronomy & Astrophysics manuscript no. aa60143-26
November 5, 2026
©ESO 2026

Electron temperatures derived from low-frequency radio observations of planetary nebulae

Marcin Hajduk[1], Timothy Shimwell[2,3], Glenn J. White[4,5], Marijke Haverkorn[6], Jesús A. Toalá[7], Ralf-Juergen Dettmar[8], and Martin J. Hardcastle[9]

[1] Department of Geodesy, Faculty of Geoengineering, University of Warmia and Mazury, ul. Oczapowskiego 2, 10-719 Olsztyn, Poland
e-mail: marcin.hajduk@uwm.edu.pl
[2] Leiden Observatory, Leiden University, PO Box 9513 2300 RA Leiden, The Netherlands
[3] ASTRON, The Netherlands Institute for Radio Astronomy, Postbus 2 NL-7990 AA Dwingeloo, The Netherlands
[4] School of Physical Sciences, The Open University, Walton Hall, Milton Keynes, MK7 6AA, UK
[5] RAL Space, STFC Rutherford Appleton Laboratory, Chilton, Didcot, Oxfordshire, OX11 0QX, UK
[6] Department of Astrophysics/IMAPP, Radboud University, PO Box 9010, 6500 GL Nijmegen, The Netherlands
[7] Instituto de Radioastronomía y Astrofísica, Universidad Nacional Autónoma de México, Morelia 58089, Mich., Mexico
[8] Ruhr University Bochum, Faculty of Physics and Astronomy, Astronomical Institute (AIRUB), 44780 Bochum, Germany
[9] Department of Physics, Astronomy and Mathematics, University of Hertfordshire, College Lane, Hatfield AL10 9AB, UK

Received September 15, 1996; accepted March 16, 1997

ABSTRACT

Context. Planetary nebulae are formed around low- and intermediate mass stars after the asymptotic giant phase and before the extinction of thermonuclear reactions. Chemical abundances and electron temperatures of planetary nebulae show a dichotomy known as an abundance and temperature discrepancy. Collisionally excited lines show higher temperatures and lower abundances compared to recombination lines. This is explained by the presence of two ionized components: a hot ionized gas and clumps of a cold, metal rich gas of unknown origin.
Aims. We aim to map radio free-free emission to determine electron temperatures across a sample of planetary nebulae to compare it with other methods to check if it traces the hot or cold component. We also aim to verify the lower radio extinction from the radio data compared to extinction determined from the Balmer decrement.
Methods. We cross-matched the LoTSS-DR3 catalogue with existing catalogues of Galactic planetary nebulae, and archival radio and optical surveys. We fitted free-free and power law spectra to the radio spectra. Determination of the electron temperatures requires observation of low-frequency turnover which marks the transition from optically thin to optically thick emission. We combined our radio observations and optical emission lines to derive radio extinction.
Results. We identified 198 planetary nebulae that are detected in LoTSS DR3 maps. We determined the emission mechanism for 147 PNe based on their radio spectra. We determined the electron temperatures for 62 planetary nebulae from optically thick thermal free-free emission. The temperatures are significantly lower than those derived from collisionally excited lines and are consistent with temperatures derived from helium recombination lines. It indicates that radio observations trace a cold ionized component in planetary nebulae. The interstellar extinction determined using interpolated 5 GHz fluxes and electron temperatures is consistent with extinction determined from Balmer line ratios. Non-thermal emission is observed in the largest and low-surface brightness planetary nebulae.

Key words. ISM: planetary nebulae: general – stars: AGB and post-AGB – Stars: evolution – Stars: winds, outflows

1. Introduction

Planetary nebulae (PNe) are formed during the evolution of low- and intermediate-mass stars ($\sim 1 - 8\,M_{\odot}$). At the final stage dust forms in the loosely bound envelope asymptotic giant star. Mass loss enhanced by pulsations and dust formation removes the outer envelope (Vassiliadis & Wood 1993). When the temperature of the exposed core rises above 20–30 kK the star ionizes the envelope. When thermonuclear reactions extinct the ejected nebula disperses into the interstellar medium and the central star becomes a white dwarf (Herwig 2005).

PNe contribute significantly to the chemical evolution of the Galaxy (Kwitter & Henry 2022) by transporting products of stellar nucleosynthesis in the AGB phase to the interstellar medium via wind (carbon and nitrogen, s-process elements). Due to the well defined cutoff in [O III] 5007 Å line luminosity PNe may serve as a ladder in the distance scale (Gesicki et al. 2018). Thanks to their bright emission lines, they can be used to determine the rotation curve and mass distribution in galaxies (Amaral et al. 1996).

PNe emit in radio wavelengths primarily via free-free emission. Their radio fluxes can be used for setting a statistical distance scale to PNe (Zhang 1995). Secular changes of their flux density reflect evolution of the central star

and nebular expansion (Zijlstra et al. 2008). Radio emission can be used to determine the electron temperature (Hajduk et al. 2021), and the ionized mass distribution (Siódmiak & Tylenda 2001). Radio observations of PNe can be used to predict dereddened Hα or Hβ flux and measure interstellar extinction in combination with the observed optical line fluxes (Tylenda et al. 1992).

The free-free thermal emission flux S_ν of a PN with electron temperature T_e at frequency ν is given by the equation (Rybicki & Lightman 1979):

$$S_\nu = \frac{2\nu^2 k T_\mathrm{e}}{c^2}(1 - e^{-\tau_\nu})\Omega \quad (1)$$

where Ω is the solid angle, k - Boltzmann constant, and c - the speed of light (Olnon 1975). τ_ν is the optical depth of the PN given by

$$\tau_\nu = 0.08235 \times T_\mathrm{e}^{-1.35}\, \nu^{-2.1} EM \quad (2)$$

where EM denotes the emission measure. Optically-thin radio flux depends on the emission measure and has a spectral index of -0.1 (Olnon 1975). At high frequencies dust emission can dominate the spectral energy distribution.

On the other hand, optically-thick radio emission depends on electron temperature and produces a spectral index of +2.0.

Partially optically thick plasma produces a spectral index between -0.1 and 2. A spectral index below -0.1 indicates non-thermal emission, or mixture of thermal and non-thermal emission (Hajduk et al. 2018).

Optically-thick radio emission enables us to measure electron temperatures in PNe from the Rayleigh-Jeans law, independently from assumptions on electron density, energy distribution, abundances or recombination ratios (Nicholls et al. 2012). In this paper we combined new radio observations from the LoTSS survey at 144 MHz with other radio surveys to determine radio emission mechanisms and, where applicable, to determine the electron temperatures in a sample of PNe.

2. Observations and identification of planetary nebulae in radio surveys

The LOFAR Two-metre Sky Survey (LoTSS) project (Shimwell et al. 2022) provided radio maps at 128–160 MHz (average frequency of 144 MHz), a resolution of 6 arcsec for pointings at declination $> 10°$ and 9 arcsec for declination $< 10°$ and a median sensitivity of 92 μJy. We used the LoTSS Data Release 3 (DR 3) observations which cover about 88% of northern sky (Shimwell et al. 2026b).

We made a position match of the LoTSS-DR3 source catalogue with the Hong Kong/AAO/Strasbourg Hα planetary nebula database (HASH; Parker et al. 2016). The HASH catalogue includes 440 true, 60 possible and 60 likely PNe in the LoTSS fields. The positions in the HASH catalogue correspond to centroid on optical images which can be offset from the catalogued radio position due to different surface brightness distribution of PNe in different parts of electromagnetic spectrum. We therefore used a 180 arcsec search radius to ensure that the optical match is found for all PNe that are detected in radio. In total, 207 matches were found.

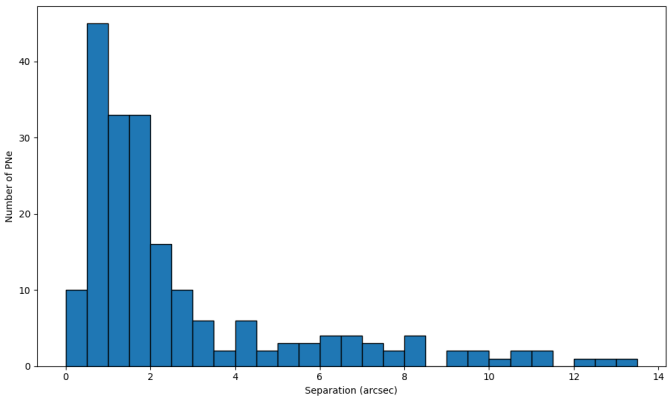


Fig. 1. Separations between the positions of PNe and LoTSS DR3 sources.

Table 1. Flux densities and sizes for extended PNe not included in the LOFAR DR3 catalogue.

Name	Flux dens. [mJy]	Size [arcsec]	PA [deg.]
Abell 59	31.08 ± 1.81	40.2×21.3	-176
NGC 1514	272.15 ± 3.26	82.3×73.7	50
NGC 3587	109.82 ± 1.36	92.7×84.5	72
NGC 6842	41.40 ± 1.34	39.3×31.8	134
NGC 6853	398.12 ± 8.09	59.8×32.0	128
NGC 7048	45.62 ± 1.60	35.8×35.0	60
Sh 2-71	67.99 ± 3.84	53.8×46.7	158

The histogram of positional offsets between the PNe and LoTSS DR3 sources is presented in Fig. 1. It shows a maximum below 1 arcsec with a wide tail toward larger separations. This is caused by PNe with lower signal-to-noise ratio and different surface brightness distribution of radio and optical emission (Callingham et al. 2019).

We inspected each LoTSS-DR3 - HASH match to minimise contamination from background objects and ensure that the recorded matches are genuine. We removed radio matches which showed morphology and brightness which suggested Active Galactic Nuclei (AGNs) and other matches suspected of being background objects. This included radio counterparts which showed an emission with different morphology and size.

The detection algorithm used in the LoTSS DR3 survey depends on peak brightness threshold and may miss low surface brightness objects despite excellent sensitivity to extended emission. In order to mitigate this problem, we visually inspected all PNe within LoTSS-DR3 area. We found radio counterparts of eight PNe which were not detected in the LoTSS DR3 catalogue. The sizes, fluxes and images of the PNe not included in the LOFAR DR3 are presented in Table 1 and Fig. A1.

After selecting a sample of PNe, we examined the flux densities determined in LoTSS-DR3. Flux densities were taken from the Gaussian fitting to the source. This could give wrong results for extended objects whose surface strength distribution can be far from Gaussian. We determined flux densities from the images integrating their flux density in the region above 2σ of the background. Both methods gave results consistent with 10%, and we used flux densities from the LoTSS-DR3 catalogue.

Table 2. Radio surveys used for spectral analysis.

Survey	Frequency	Beam size	rms [mJy/beam]	Reference
LoTSS-DR3	144 MHz	$6''$	0.07	[1]
GLEAM	72–231 MHz	$2'$	10	[2]
WENSS	325 MHz	$54'' \times 54'' \,\mathrm{cosec}(\delta)$	3.6	[3]
RACS-low	887.5 MHz	$25'' \times 25''$	0.275	[4]
RACS-mid	1367.5 MHz	$10'' \times 8''$	0.198	[4]
RACS-high	1655.5 MHz	$8.6'' \times 6.3''$	0.209	[5]
NVSS	1.4 GHz	$45''$	0.45	[6]
THOR	1–2 GHz	$25''$	0.5	[7]
G88	1.5 GHz	$4''$	$\sim$10	[8]
VLASS	2–4 GHz	$2.5''$	0.12	[9]
CORNISH	5 GHz	$1.5''$	0.4	[10]
A90	5 GHz	$3.5''$	25	[11]
A91	15 GHz	$1.5''$	15	[12]
AMI	15.75 GHz	$3'$	3	[13]
Z89	1.4, 5, 15 GHz	see reference	25	[14]

References. [1] Shimwell et al. (2026b); [2] Hurley-Walker et al. (2017); [3] Rengelink et al. (1997); [4] Hale et al. (2021); [5] Duchesne et al. (2025); [6] Condon et al. (1998); [7] Bihr et al. (2016); [8] Garwood et al. (1988); [9] Gordon et al. (2021); [10] Irabor et al. (2018); [11] Aaquist & Kwok (1990); [12] Aaquist & Kwok (1991); [13] Perrott et al. (2015); [14] Zijlstra et al. (1989).

We calculated 144 MHz radii using deconvolved minor and major diameter from the Gaussian fit, provided by LoTSS-DR3 catalogue. Then we applied a correction factor from van Hoof (2000) using a shell model with the outer-to inner radius ratio of 2.

We combined LoTSS data with other radio observations (Table 2) to analyze their spectra and determine the radio emission mechanisms. We used a matching radius of 30 arcsec to the LoTSS DR3 coordinates. We used data from interferometric surveys to reduce the possibility of blending with background sources. We focused on synchrotron and free-free emission. We did not use observations above $\sim$ 16 GHz to avoid a contribution of thermal emission of dust which becomes dominant at the submilimeter range. In the case of the Arcminute Microkelvin Imager Galactic Plane Survey (AMI) at 16 GHz we used integrated flux for extended sources and peak flux for point sources, as suggested by the authors (Perrott et al. 2015).

3. Determination of the radio emission mechanism

PNe emit free-free radio emission due to acceleration of thermal electrons in the electric field of ions. Non-thermal emission is associated with transition from proto planetary nebulae to PNe (Bains et al. 2009), but has also been found in a few PNe (Suárez et al. 2015; Hajduk et al. 2024). Thus we fitted the observed radio spectra with these two mechanisms, which could be distinguished on the basis of their spectral index. Thermal emission produces a spectral index between -0.1 and 2 and non-thermal emission produces a negative spectral index.

We fitted a power law and thermal free-free emission (equation 1) for the PNe which had at least two data points. We used radio diameters from LOFAR observations, and for unresolved sources we used optical diameters from HASH catalogue (Table **??**). Emission measure and electron temperature may be biased for PNe unresolved in radio, so we do not list the determined parameters. All spectral fits are performed using a non-linear weighted least-squares χ^2 minimisation. The associated observational uncertainties were taken from surveys or - if not available - adopted at the level of 15%. Free-free fit constrained T_e and EM well if at least one data point represented optically thick and optically thin regime. The initial parameter range was $10 < T_\mathrm{e} < 20000$K and $10^3 < EM < 3 \times 10^8\,\mathrm{cm}^{-6}\,\mathrm{pc}$. We extend range of values to very low T_e to ensure that all the PNe are fitted. The T_e values from the lower boundary do not have physical sense, but may be formarly derived in the case of a large error on the nebular diameter. Uncertainties on T_e and EM are derived from the covariance matrix returned by the fitting procedure, calculated for the best-fit solution. We took into account the finite bandwidth of the LoTSS observations, which may be significant in the case of steep spectra (e.g. for high optical depth at 120-168 MHz). We ignored finite bandwidth for other surveys, since it was much narrower than in LoTSS and in most cases spectra were relatively flat at frequencies above 144 MHz.

We calculated reduced χ^2 for all PNe for both models. We visually inspected spectra showing reduced $\chi^2 > 3$. Large χ^2 could be caused by outliers (systemic errors), different spectral characteristics from the two assumed models or intrinsic source variability. PNe rarely show maser emission or other spectral features which could significantly contribute to radio continuum flux.

We identified data points affected by systemic errors (outliers). We removed 20 VLASS data points for PNe larger than about 30 arcsec, which were underestimated due to a drop of the survey sensitivity to extended structures. Zijlstra et al. (1989) underestimated 5 GHz flux density for four faint PNe (Pottasch & Zijlstra 1994). We removed a few outliers in the spectra caused by blending with background sources due to insufficient spatial resolution in the NVSS survey and a few outliers in the THOR survey. Finally, we removed a few high-frequency outliers due to possible contribution of thermally emitting dust. For spectra containing more than one outlier, we examined source variability as a potential reason. We assessed the statistical significance of the fitted linear trends by testing the null hypothesis that the slope is zero. The two-sided p-value was calculated using Student's t-distribution with $N - 2$ de-

Table 3. Classification criteria for spectral types.

Type	$\chi^2_{\rm ff}$	$\chi^2_{\rm pl}$	SI	# PNe
Thick	<3.5	$>\chi^2_{\rm ff}+1.5$		66
Intermediate	<3.5	<3.5	SI$-\delta$SI>-0.1	40
Thin	<3.5	<3.5	$\lvert$SI$+0.1\rvert\leq\delta$SI	21
Nonthermal		<3.5	SI$+\delta$SI<-0.1	20
Unclassified	>3.5	>3.5		51

grees of freedom, where N is the number of measurements included in the fit. We considered trends with $p < 0.05$ statistically significant. According to this criterion, 14 objects exhibit statistically significant linear trends over the observational time span.

We assigned the sources to five categories based on their spectra: thick, intermediate (partially thick), thin, nonthermal, and unclassified. The first three categories are associated with thermal free-free emission. The classification criteria are summarized in Table 3.

We classified 66 PNe for which the difference between chi squared for thermal and powerlaw fits $\chi^2_{pl} - \chi^2_{th} > 1.5$ as optically thick thermal PNe. These were cases where the spectra were well sampled with low-frequency turnovers clearly visible (i.e. when the PN spectrum becomes optically thick at low frequencies, e.g. Fig. 2).

For 21 PNe, the powerlaw fit gave $\chi^2_{pl} < 3.5$ and their spectral index was consistent with -0.1 indicating optically thin emission.

We classified 40 PNe as intermediate where a powerlaw model gave positive spectral index. 20 PNe showed nonthermal emission with a spectral index significantly less than -0.1.

For 27 PNe we could not indicate the source of emission since both free-free and powerlaw fit gave $\chi^2 > 3.5$. The potential reasons could be variability, systematic errors, different emission mechanism or superposition of thermal and nonthermal emission. It is difficult to verify variability, as observations were taken at different frequencies with different instruments. We analyzed time variability of PNe assuming that they are optically thin above 0.9 GHz (thus their spectra are almost flat). 14 PNe shows significant trends (online material). This includes K 3-35, a young nebula which shows water maser emission (Tafoya et al. 2007). Velázquez et al. (2007) observed precessing ionized jet in radio. The decrease of the flux may indicate recombination of the jet, which could be ejected in a short timescale transient (common envelope phase of evolution). Nine PNe were not detected in other surveys and fifteen had only two datapoints. Two datapoints are sufficient to make a fit but do not enable us for robust discrimination between different emission mechanisms. In total, 51 spectra were not classified.

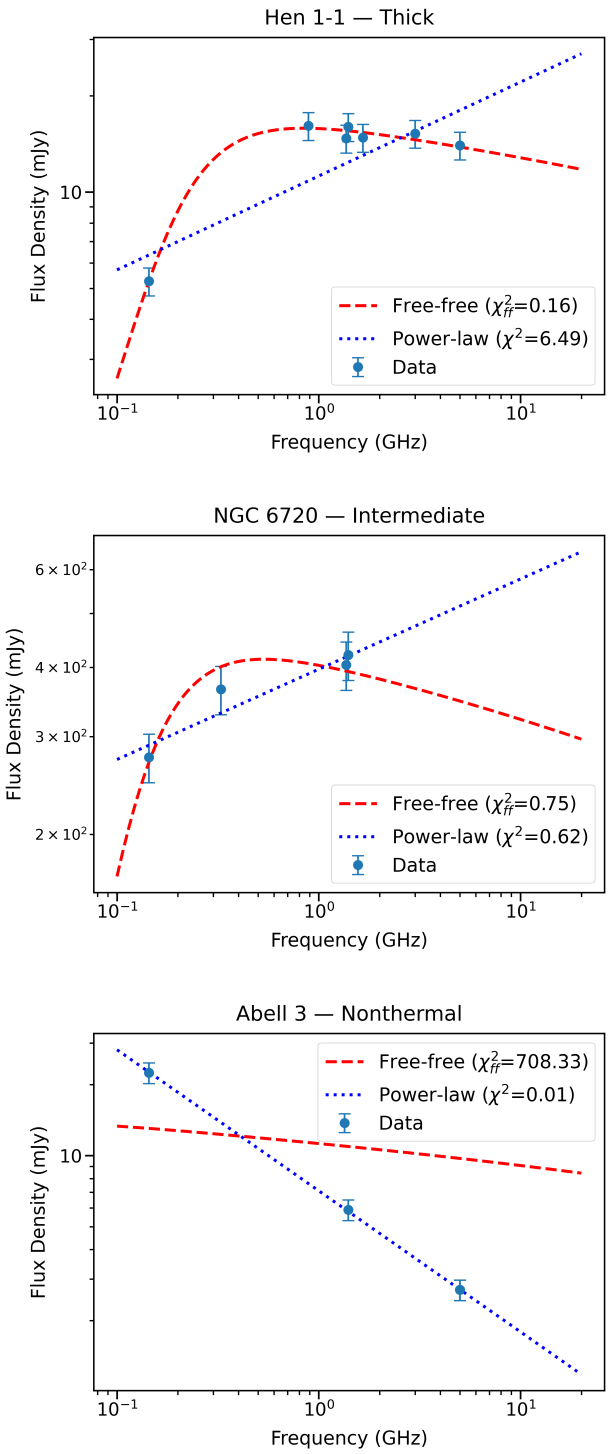


Fig. 2. Comparison of free-free and powerlaw fits for the PN Hen 1-1, NGC 6720 and Abell 3.

4. Electron temperatures

We calculated nebular sizes in order to determine the surface brightness and electron temperatures. A comparison of the 144 MHz and optical sizes is shown in Fig. 3. The agreement between the 144 MHz and optical sizes is better for higher S/N ratio. Optically thick diameters are smaller than optical sizes for sizes smaller than restoring beam for LoTSS DR3 (6 or 9 arcsec for low declinations). The comparison of sizes for different groups is shown in Fig. 4. Non-thermal sources are smaller than optical ones. For resolved PNe, non-thermal radio emission fills all the volume of the hot bubble or exists on the boundary of the hot bubble with the dense shell (Hajduk et al. 2025). There are two extreme outliers in the optically thick group. KK 26 has much larger optical diameter from radio diameter. It consists of extended lobes and a compact elliptical ring surrounding the central star (Guerrero et al. 2013). Radio observations measure this

ring. Bl 2-1 is about 10 times more extended in radio than in optical (1.6 arcsec). It is weak with S/N of the peak flux of 3.2. Gaussian fitting extended to background. However, the 4 data points at higher frequency show a spectrum typical for a PN, so we retain it in Table A1 and Table B1, but marked it as unreliable.

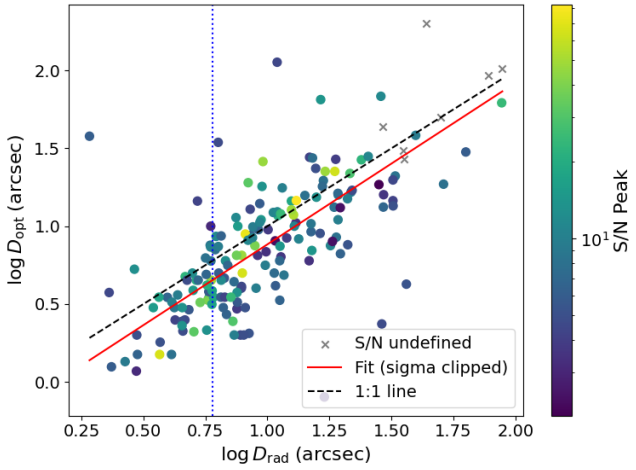


Fig. 3. Comparison of the deconvolved 144 MHz and optical diameters. The vertical line marks 6 arcsec diameter, corresponding to a restoring beam of the 144 MHz survey above declination 10 deg. The restoring beam for below 10 deg is 9 arcsec. The black dashed line plots the 1:1 line. The colors of the symbols denote peak signal-to-noise ratio.

Our calculation of electron temperature assumes that the entire solid angle produces radio emission, i.e. surface filling factor is 1. The mean volume filling factor in PNe is $0.3 - 0.4$. The observed range covers values from 0.01 to 1 (Boffi & Stanghellini 1994). Optically thick PNe tend to have larger volume filling factors. Volume filling factor combines the effect caused by geometrical structure (e.g. large inner cavity) and smaller scale structures (e.g. clumps). The same volume filling factor may result in different surface filling factor, depending on the size and distribution of the ionized clumps.

In the case of a large inner void, the optical depth would be decreased in the lines of sight passing through the void which results in a ring like appearance, e.g. in NGC 6720, NGC 1501 or IC 289. When whole PN becomes optically thick, the images resemble a disk, e.g. in NGC 6543, NGC 6826 or NGC 7662.

Clumps that have angular dimensions larger than the telescope beam would remain invisible in the image. Lines of sight that would not pass through clumps would not contribute to the observed radio flux. The calculated average electron temperature would be averaged over clumps and voids. However, randomly distributed clumps may fill projected area, thus projected area covering fraction can be close to 1 even though volume filling factor would be much lower.

The projected area covering fraction, f_A, was estimated assuming a random distribution of spherical clumps of identical radius r_c within a spherical nebula of radius R. The mean number of clumps intercepted along a line of sight is approximated by the mean projected covering optical depth,

$$\tau_A = n_c \pi r_c^2 \langle L \rangle = \frac{3}{2} f_V \frac{R}{r_c},$$

where $n_c = 3 f_V / (4\pi r_c^3)$ is the clump number density and $\langle L \rangle = 4R/3$ is the mean chord length through a sphere for randomly distributed parallel lines of sight. Assuming a Poisson distribution of clumps, the projected area covering fraction is then

$$f_A = 1 - \exp(-\tau_A) = 1 - \exp\left(-\frac{3}{2} f_V \frac{R}{r_c}\right).$$

Fig. 5 shows f_A as a function of the relative clump radius r_c/R for different volume filling factors.

In the case of clump size of 0.001 of the diameter surface filling factor becomes unity for volume filling factors greater than 0.003. Optical observations show small scale cometary knots of the size of 0.001 of radius (O'Dell et al. 2007).

If only part of the PN would be optically thick, the spectrum would have spectral index < 2 in optically thick part. Analogical situation is for ionized winds, in the case of spherically symmetric wind with constant mass loss rate results in part of the disk optically thick and part optically thin. The combination of these two results in the spectral index of 0.6. Only four optically thick PNe have a good coverage of the spectrum in the optically thick part: K 3-52, BD+30 3639, M 1-4, and NGC 6543 between 144 MHz and 327 MHz or 144 MHz and 1.4 MHz. Their spectral indices determined from two to four optically thick points at lowest frequencies ranges between 1.5 and 1.8. For a spherically symmetric model, spectral index of 1.5 and 1.8 would be produced if 7% and 2% of the projected disk had an optical depth $\tau < 1$. If part of the projected disk was partially optically thin, this would produce a systematic error in the electron temperature determination of the order of a few percent. However, optical thickness strongly depends on ν and the regions which are partially optically thin at 327 MHz or 1.4 GHz may be already optically thick at 144 MHz.

We fitted electron temperatures and emission measures using 144 MHz sizes and equation 1 (Table **??**) for optically thick PNe. We do not list the result of the fit for the objects which do not have their radii determined in LoTSS, i.e. K 3-78, IPHASX J195248, IPHAS J192553, and 2MASS J19453289. $S_\nu \propto T_e$ in optically thick regime, while $S_\nu \propto T_e^{-0.35} EM$ in optically thin part of the spectrum. Thus, solution is degenerate for spectra which do not show a turnover (emission measure and electron temperature cannot be determined independently).

We calculated the optical depth at 5 GHz and 144 MHz from the fitted spectra. The optical depth at 5 GHz was found to be negligible in most cases, reaching values of 0.3 in two PNe. For PNe optically thick at 144 MHz, the brightness temperature is equal to the electron temperature. Electron temperature maps are available in the Online material. Most of the PNe are not sufficiently well resolved at 144 MHz to allow us to study spatial variations of electron temperature. In some cases the 144 MHz brightness distribution is not uniform, e.g. in NGC 2392. This may result from local differences in the electron temperature. However, it is also possible that the outer regions have lower optical depth, e.g. $\tau_{144MHz} \sim 2$ for which the

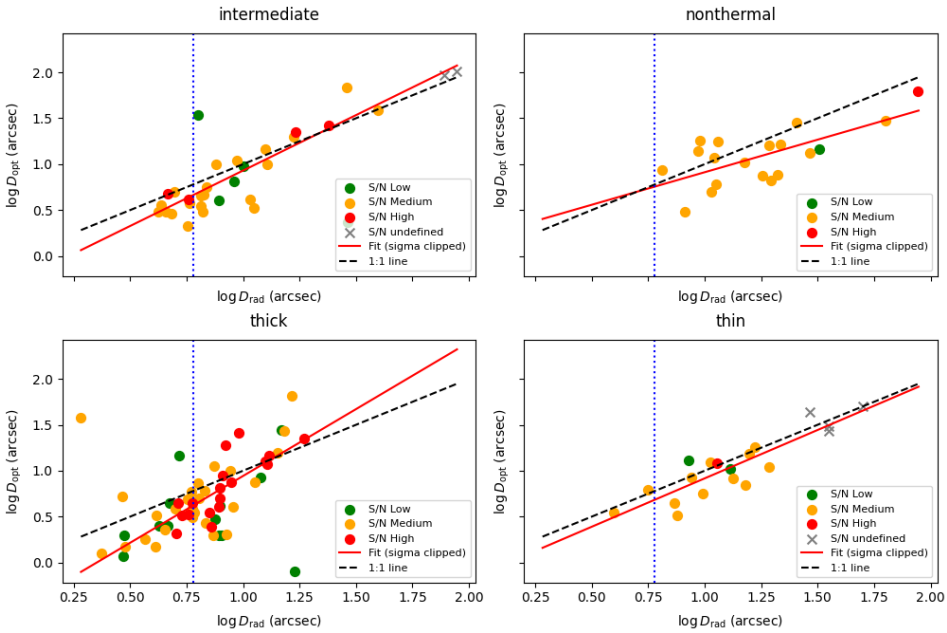


Fig. 4. Comparison of the deconvolved 144 MHz (R_{DC}) and optical (D_{opt}) diameters for different groups of objects: nonthermal, optically thick, intermediate, and optically thin.

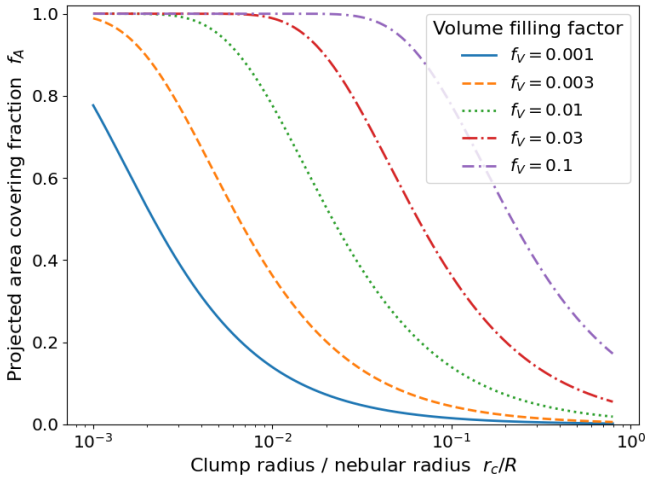


Fig. 5. Dependence of part of the projected area covered by clumps on the clump size and filling factor.

brightness temperature is lower than the electron temperature by 15%. Comparison of the 144 MHz map with a map at higher frequency, and similar spatial resolution, would confirm if the outer regions are optically thick.

We compared the radio electron temperatures with electron temperatures derived from atomic line flux ratios. For nebulae with temperature measurements reported by multiple authors, we adopted the average of the published values. The electron temperatures derived from atomic lines show the well known dichotomy. The [O III] λ4363/5007 line flux ratio and other collisionally excited lines indicate the highest observed temperatures. The Balmer discontinuity is more sensitive to regions with lower electron temperatures. Optical recombination lines show even lower temperatures from the Balmer discontinuity, which indicates inhomogeneities in density and chemical abundances within nebular shells (Corradi et al. 2015).

The electron temperatures derived from radio observations of optically thick PNe are on average lower by 5700 ± 900 K than electron temperatures measured using collisionally excited lines, e.g. [O III] λ4363/5007 (Fig. 6). This is expected since temperatures derived from collisionally excited lines are weighted toward hotter regions, where these lines form more effectively. Temperatures derived from radio emission are weighted toward colder regions as the optical depth depends on $T_e^{-1.35}$.

Temperatures determined from radio observations are on average 3100 ± 600 K lower than temperatures derived from the Balmer discontinuity (Fig. 6) after removing two outliers on the basis of 3.5 σ deviation from the median. Radio temperatures agree well with temperatures derived from helium recombination line ratios λ7281/6678, λ7281/5876, λ5876/4471 and λ6678/4471. The difference is 200 ± 1400 K. Radio temperatures are higher than temperatures derived from O recombination lines by 800 ± 2000 K, which is not statistically significant due to large scatter of the values. This may indicate that radio emission traces a similar medium as He recombination lines in most of the PNe.

5. Interstellar extinction

Free-free optically thin radio emission can be combined with Balmer line fluxes (most frequently Hβ) to measure the absolute extinction toward a PN. The radio flux is not affected by interstellar extinction and can be used to calculate expected unreddened Hβ flux. Comparison of the expected and observed Hβ fluxes gives information on extinction at 4861 Å(Acker et al. 1992):

$$C_{\rm rad} = \log \frac{F(H\beta_{exp})}{F(H\beta_{obs})}$$

On the other hand, the observed Hα to Hβ line flux ratio is very weakly dependent on electron temperature and density for case B recombination (Pottasch 1984), which is valid for nearly all PNe. Comparison of the observed $H\alpha$ to $H\beta$ line flux ratio with theoretical ratio of 2.85 gives information on selective extinction. Absolute extinction at $H\beta$ wavelength can be derived after applying the standard

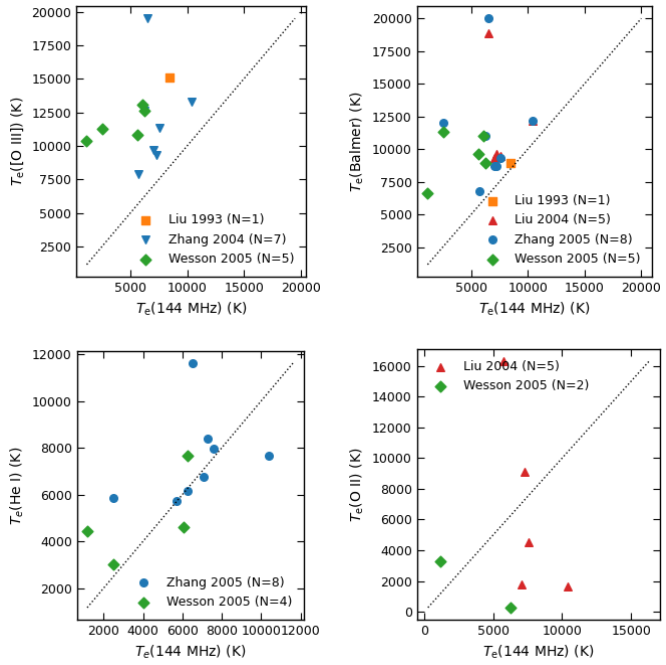


Fig. 6. Comparison of radio temperatures determined from 144 MHz brightness temperature and temperatures derived from [O III] λ5007/4363 (Liu & Danziger 1993; Zhang et al. 2004; Wesson et al. 2005), Balmer recombination (Liu & Danziger 1993; Liu et al. 2004; Zhang et al. 2005; Wesson et al. 2005), Helium recombination lines (Zhang et al. 2005; Wesson et al. 2005) and O II recombination lines (Liu et al. 2004; Wesson et al. 2005).

extinction law with the absolute to selective extinction ratio of $R_{\rm V} = 3.1$ (Cardelli et al. 1989):

$$C_{\rm opt} = 3.10 \log \frac{2.85}{F(H\alpha_{obs})/F(H\beta_{obs})}$$

Previous studies reported an excess of optical extinction $C_{\rm opt}$ with respect to the radio extinction $C_{\rm rad}$ by a factor of about 1.2 (e.g. Cahn et al. (1992), Tylenda et al. (1992), Stasińska et al. (1992)). $C_{\rm opt}$ and $C_{\rm rad}$ could be reconciled when a non-standard extinction law was adopted, i.e. $R_{\rm V} = 2.0$ instead of 3.1 (Ruffle et al. 2004). However, there is a lack of evidence for $R_{\rm V} = 2.0$ from independent studies.

We used the formula from Pottasch (1984) to calculate the expected unreddened Hβ fluxes from the observed 5 GHz flux:

$$F(H\beta_{exp}) = \frac{S_{\rm 5GHz}}{2.82 \cdot 10^{12} t^{0.53} Y} \quad (3)$$

where S_{5GHz} is given in mJy, t is electron temperature $T_e/10000K$, and $Y = 1 + \frac{n(He^+)}{n(H^+)} + 3.7\frac{n(He^{++})}{n(H^+)}$.

The 5 GHz flux was interpolated from radio SED (Table B1). We corrected the 5 GHz flux by finite optical depth τ_{5GHz} derived from radio spectra. This correction was significant only in two cases, BD+30 3639 and K 3-52. Electron temperatures were taken from modeling of radio spectra (Table B1). We used published Hβ fluxes (Acker et al. 1992) and compared them to the dereddened $F(H\beta_{exp})$ fluxes to derive extinction (so called radio extinction C_{rad}).

We compared the calculated extinction with the extinction given by Cahn et al. (1992) from observed Balmer lines ratio C_{opt} (Fig. 7). The radio extinction is consistent with the optical extinction (1:1 relation) within uncertainties, although some excess of radio extinction is visible. The reason for the discrepancy may be that in Equation 3 we used electron temperature from outer regions of the PN, optically thick at 144 MHz, while $S_{\rm 5GHz}$ is calculated from optically thin region (averaged over nebular volume), where inner regions with higher electron temperature can contribute.

Gómez-Llanos & Morisset (2020) performed a grid of photoionization models in which PNe were approximated with two phase gas. Cold metal-rich clumps, emitting recombination lines, were embedded in normal metallicity region. In their models, most of Hβ flux originates from the 'normal' gas.

Stasińska et al. (1992) combined radio fluxes and T_e determined from optical collisionally excited lines (CEL). T_e determined from CEL represents hot component whereas optically thin $S_{\rm 5GHz}$ flux is averaged over the PN volume. In the result, they underestimated the Hβ emission expected from radio flux. This in turn decreased radio extinction $c_{\rm rad}$.

In our study T_e on the right side of Eq. 3 is determined from radio observations and is weighted toward colder regions, which have higher optical thickness. This leads to overestimated expected Hβ flux. This can be observed as an excess of $c_{\rm rad}$ with respect to $c_{\rm opt}$ in Fig. 7.

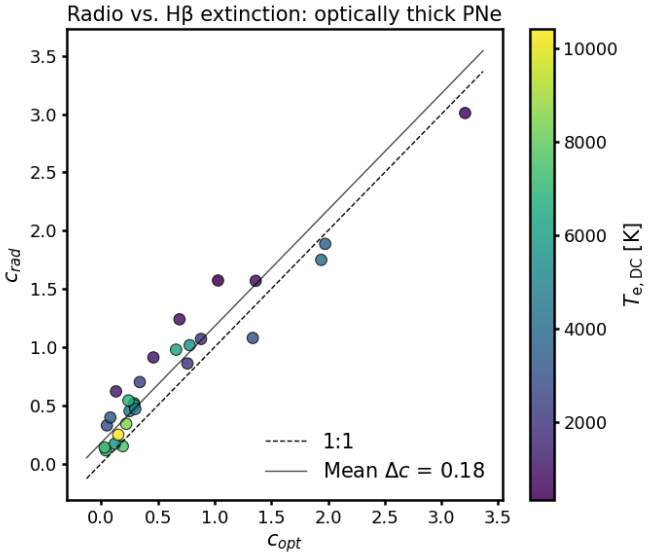


Fig. 7. Comparison of extinction determination for optically thick PNe. Color of the symbols codes the electron temperature.

6. Surface brightness

Fig. 8 shows histograms of surface brightness determined as flux density divided by the PN area for different spectral classes. The number of PNe is lower than in Table 3, because some of PNe do not have radio diameter determined, necessary for computing surface brightness. Thermal PNe show higher surface brightness than optically thin PNe. Intermediate objects are localized between optically thin and optically thick. Non-thermal PNe show the lowest surface brightness.

As the nebula expands, the surface density and the optical thickness decrease. Then the nebula becomes optically thin. Non-thermal emission becomes visible in the last

stage, possibly because it is very faint and suppressed by thermal emission at earlier stages.

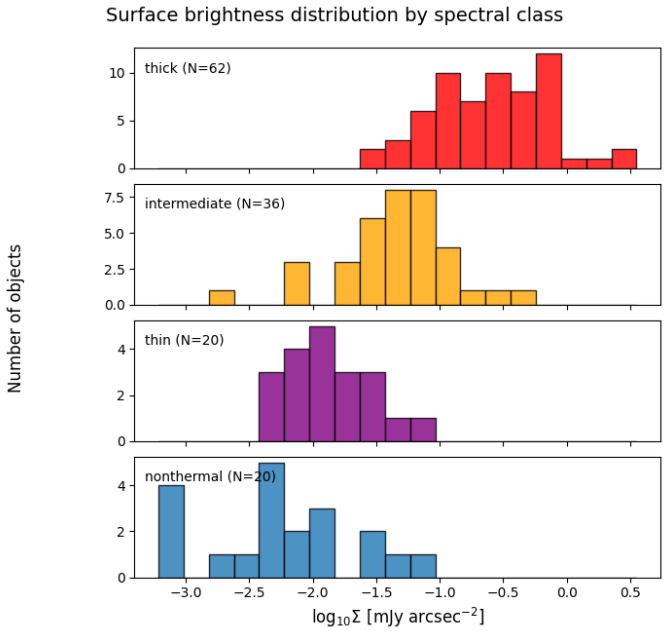


Fig. 8. Histograms of surface brightness for different spectral classification.

7. Summary

We analyzed radio observations of 198 PNe detected with LOFAR at 144 MHz (Table **??**). Low-frequency observations helped us to constrain the nature of the radio emission mechanism. We determined electron temperatures for optically thick PNe. The temperatures are significantly lower than temperatures derived from collisionally excited lines. Radio determined temperatures are well correlated with, but still lower than temperatures derived from Balmer jump and consistent with temperatures derived from helium recombination lines. This indicates that optically thick radio emission traces cold and dense regions in PNe.

Extinction determined from radio emission shows a small excess with respect to extinction determined from Balmer line ratios using electron temperatures determined from radio observations. Previous studies reported an excess of radio extinction (e.g. Cahn et al. (1992), Tylenda et al. (1992), Stasińska et al. (1992), Ruffle et al. (2004)). Pottasch & Bernard-Salas (2013) attributed this discrepancy to non-negligible optical depth at GHz frequencies. Our observations indicate that the vast majority of PNe are optically thin at GHz frequencies. However, the temperature for calculation of expected unreddened $H\beta$ flux should be derived from radio observations.

Evolved, low surface-brightness PNe show non-thermal emission. Non-thermal emission can be present in earlier stages of PN evolution, but then it is dominated by thermal emission.

8. Data availability

Spectra and images are available on Zenodo at `https://zenodo.org/records/23975208`. The original LOFAR images and catalogue are available in Shimwell et al. (2026a).

Acknowledgements. RJD acknowledges support by the BMFTR ErUM-Pro program. This research has made use of "Aladin sky atlas" developed at CDS, Strasbourg Observatory, France. Computations were carried out using the computers of Centre of Informatics Tricity Academic Supercomputer & Network.

References

Aaquist, O. B. & Kwok, S. 1990, A&AS, 84, 229
Aaquist, O. B. & Kwok, S. 1991, ApJ, 378, 599
Acker, A., Marcout, J., Ochsenbein, F., et al. 1992, The Strasbourg-ESO Catalogue of Galactic Planetary Nebulae. Parts I, II.
Amaral, L. H., Ortiz, R., Lepine, J. R. D., & Maciel, W. J. 1996, MNRAS, 281, 339
Bains, I., Cohen, M., Chapman, J. M., Deacon, R. M., & Redman, M. P. 2009, Monthly Notices of the Royal Astronomical Society, 397, 1386
Bihr, S., Johnston, K. G., Beuther, H., et al. 2016, A&A, 588, A97
Boffi, F. R. & Stanghellini, L. 1994, A&A, 284, 248
Cahn, J. H., Kaler, J. B., & Stanghellini, L. 1992, A&AS, 94, 399
Callingham, J. R., Vedantham, H. K., Pope, B. J. S., Shimwell, T. W., & LoTSS Team. 2019, Research Notes of the American Astronomical Society, 3, 37
Cardelli, J. A., Clayton, G. C., & Mathis, J. S. 1989, ApJ, 345, 245
Condon, J. J., Cotton, W. D., Greisen, E. W., et al. 1998, AJ, 115, 1693
Corradi, R. L. M., García-Rojas, J., Jones, D., & Rodríguez-Gil, P. 2015, ApJ, 803, 99
Duchesne, S., Ross, K., Thomson, A. J. M., et al. 2025, PASA, 42, 38
Garwood, R. W., Perley, R. A., Dickey, J. M., & Murray, M. A. 1988, AJ, 96, 1655
Gesicki, K., Zijlstra, A. A., & Miller Bertolami, M. M. 2018, Nature Astronomy, 2, 580
Gómez-Llanos, V. & Morisset, C. 2020, MNRAS, 497, 3363
Gordon, Y. A., Boyce, M. M., O'Dea, C. P., et al. 2021, Astrophysical Journal Supplement Series, 255, 30
Guerrero, M. A., Miranda, L. F., Ramos-Larios, G., & Vázquez, R. 2013, A&A, 551, A53
Hajduk, M., Haverkorn, M., Shimwell, T., et al. 2021, ApJ, 919, 121
Hajduk, M., Shimwell, T., White, G., et al. 2025, A&A, 703, L5
Hajduk, M., van Hoof, P. A. M., Śniadkowska, K., et al. 2018, MNRAS, 479, 5657
Hajduk, M., van Hoof, P. A. M., Zijlstra, A. A., et al. 2024, Astronomy & Astrophysics, 688, L21
Hale, C. L., McConnell, D., Thomson, A. J. M., et al. 2021, PASA, 38, e058
Herwig, F. 2005, ARA&A, 43, 435
Hurley-Walker, N., Callingham, J. R., Hancock, P. J., et al. 2017, MNRAS, 464, 1146
Irabor, T., Hoare, M. G., Oudmaijer, R. D., et al. 2018, MNRAS, 480, 2423
Kwitter, K. B. & Henry, R. B. C. 2022, PASP, 134, 022001
Liu, X.-W. & Danziger, J. 1993, MNRAS, 263, 256
Liu, Y., Liu, X.-W., Barlow, M. J., & Luo, S.-G. 2004, MNRAS, 353, 1251
Nicholls, D. C., Dopita, M. A., & Sutherland, R. S. 2012, ApJ, 752, 148
O'Dell, C. R., Henney, W. J., & Ferland, G. J. 2007, AJ, 133, 2343
Olnon, F. M. 1975, A&A, 39, 217
Parker, Q. A., Bojičić, I. S., & Frew, D. J. 2016, in Journal of Physics Conference Series, Vol. 728, Journal of Physics Conference Series (IOP), 032008
Perrott, Y. C., Scaife, A. M. M., Green, D. A., et al. 2015, MNRAS, 453, 1396
Pottasch, S. R. 1984, Planetary nebulae. A study of late stages of stellar evolution, Vol. 107
Pottasch, S. R. & Bernard-Salas, J. 2013, A&A, 550, A35
Pottasch, S. R. & Zijlstra, A. A. 1994, A&A, 289, 261
Rengelink, R. B., Tang, Y., de Bruyn, A. G., et al. 1997, A&AS, 124, 259
Ruffle, P. M. E., Zijlstra, A. A., Walsh, J. R., et al. 2004, MNRAS, 353, 796
Rybicki, G. B. & Lightman, A. P. 1979, Radiative processes in astrophysics
Shimwell, T. W., Hardcastle, M. J., Tasse, C., et al. 2022, A&A, 659, A1

Shimwell, T. W., Hardcastle, M. J., Tasse, C., et al. 2026a, VizieR Online Data Catalog: LOFAR Two-metre Sky Survey (LoTSS) DR3 (Shimwell+, 2026), VizieR On-line Data Catalog: J/A+A/707/A198. Originally published in: 2026A&A...707A.198S
Shimwell, T. W., Hardcastle, M. J., Tasse, C., et al. 2026b, A&A, 707, A198
Siódmiak, N. & Tylenda, R. 2001, A&A, 373, 1032
Stasińska, G., Tylenda, R., Acker, A., & Stenholm, B. 1992, A&A, 266, 486
Suárez, O., Gómez, J. F., Bendjoya, P., et al. 2015, ApJ, 806, 105
Tafoya, D., Gómez, Y., Anglada, G., et al. 2007, AJ, 133, 364
Tylenda, R., Acker, A., Stenholm, B., & Koeppen, J. 1992, A&AS, 95, 337
van Hoof, P. A. M. 2000, MNRAS, 314, 99
Vassiliadis, E. & Wood, P. R. 1993, ApJ, 413, 641
Velázquez, P. F., Gómez, Y., Esquivel, A., & Raga, A. C. 2007, MNRAS, 382, 1965
Wesson, R., Liu, X.-W., & Barlow, M. J. 2005, MNRAS, 362, 424
Zhang, C. Y. 1995, ApJS, 98, 659
Zhang, Y., Liu, X.-W., Liu, Y., & Rubin, R. H. 2005, MNRAS, 358, 457
Zhang, Y., Liu, X.-W., Wesson, R., et al. 2004, MNRAS, 351, 935
Zijlstra, A. A., Pottasch, S. R., & Bignell, C. 1989, A&AS, 79, 329
Zijlstra, A. A., van Hoof, P. A. M., & Perley, R. A. 2008, ApJ, 681, 1296